

# Photometric redshift estimation of galaxies in the DESI Legacy Imaging Surveys

Changhua Li<sup>1,2,3</sup>, Yanxia Zhang<sup>1,4\*</sup>, Chenzhou Cui<sup>1,3†</sup>, Dongwei Fan<sup>1,3</sup>,  
Yongheng Zhao<sup>1</sup>, Xue-Bing Wu<sup>5,6</sup>, Jing-Yi Zhang<sup>1</sup>, Yihan Tao<sup>1,3</sup>, Jun Han<sup>1,3</sup>,  
Yunfei Xu<sup>1,3</sup>, Shanshan Li<sup>1,2,3</sup>, Linying Mi<sup>1,3</sup>, Boliang He<sup>1,2,3</sup>, Zihan Kang<sup>1,2</sup>,  
Youfen Wang<sup>1,3</sup>, Hanxi Yang<sup>1,3</sup> and Sisi Yang<sup>1,3</sup>

<sup>1</sup> National Astronomical Observatories, Beijing, 100101, China

<sup>2</sup> University of Chinese Academy of Sciences, Beijing 100049, China

<sup>3</sup> National Astronomical Data Center, Beijing 100101, China

<sup>4</sup> CAS Key Laboratory of Optical Astronomy, National Astronomical Observatories, Beijing, 100101, China

<sup>5</sup> Department of Astronomy, School of Physics, Peking University, Beijing 100871, China

<sup>6</sup> Kavli Institute for Astronomy and Astrophysics, Peking University, Beijing 100871, China

Released 2002 Xxxxx XX

## ABSTRACT

The accurate estimation of photometric redshifts plays a crucial role in accomplishing science objectives of the large survey projects. The template-fitting and machine learning are the two main types of methods applied currently. Based on the training set obtained by cross-correlating the DESI Legacy Imaging Surveys DR9 galaxy catalogue and SDSS DR16 galaxy catalogue, the two kinds of methods are used and optimized, such as EAZY for template-fitting approach and CATBOOST for machine learning. Then the created models are tested by the cross-matched samples of the DESI Legacy Imaging Surveys DR9 galaxy catalogue with LAMOST DR7, GAMA DR3 and WiggleZ galaxy catalogues. Moreover three machine learning methods (CATBOOST, Multi-Layer Perceptron and Random Forest) are compared, CATBOOST shows its superiority for our case. By feature selection and optimization of model parameters, CATBOOST can obtain higher accuracy with optical and infrared photometric information, the best performance ( $\text{MSE} = 0.0032$ ,  $\sigma_{\text{NMAD}} = 0.0156$  and  $O = 0.88$  per cent) with  $g \leq 24.0$ ,  $r \leq 23.4$  and  $z \leq 22.5$  is achieved. But EAZY can provide more accurate photometric redshift estimation for high redshift galaxies, especially beyond the redshift range of training sample. Finally, we finish the redshift estimation of all DESI DR9 galaxies with CATBOOST and EAZY, which will contribute to the further study of galaxies and their properties.

**Key words:** Astronomical data bases: catalogues - surveys - Galaxies: general - galaxies: photometry - galaxies: distances and redshifts

## 1 INTRODUCTION

With the development and use of many large-scale survey telescopes, like the Sloan Digital Sky Survey (SDSS; York et al. 2000), the Kilo-Degree Survey (KiDS; de Jong et al. 2013), the Panoramic Survey Telescope & Rapid Response System (Pan-STARRS; Chambers et al. 2016), and the Dark Energy Survey (DES; The DES Collaboration, 2005), multi-band photometries of

a large number of galaxies have been obtained. Estimating the photometric redshifts of galaxies is one of the most important steps for probing cosmology and will greatly improve the scientific output of survey telescopes. Since Puschell et al. (1982) first proposed photometric redshift, photometric redshift estimation technologies have been developed rapidly and have become an important issue of astronomical research.

At present, there are many common algorithms for photometric redshift estimation, they can be generally divided into two categories: template-fitting and machine learning methods. The template-fitting methods

\* Email: zyx@bao.ac.cn

† Email: ccz@bao.ac.cn

establish the relationship between synthetic magnitudes (flux) and redshifts by a series of spectral energy distribution templates. The earliest published photometric redshift codes include LePhare (Arnouts et al. 1999), BPZ (Bayesian photometric Redshifts; Benitez et al. 2000) and HYPERZ (Bolzonella et al. 2000). Since then more photometric redshift codes have been devised and published, such as PhotoZ Bayesian (Bender et al. 2001), Z-PEG (Le Borgne & Rocca-Volmerange, 2002), IMPZ (Babbedge et al. 2004), ZEBRA (Feldmann, et al. 2006) and EAZY (Brammer et al. 2008). Generally speaking, machine learning algorithms are to find the relation between photometric information and redshifts based on known samples, which is called as training. With this relation, the model is established, it can be used to map the same observable data. Early machine learning approaches include polynomial fitting (Connolly et al. 1995), and  $k$  nearest neighbours (kNN; Csabai et al. 2003; Zhang et al. 2013; Curran et al. 2021; Nishizawa et al. 2020;). Afterwards, with increasingly powerful computing and storage capabilities, many powerful machine learning algorithms have emerged and were widely applied to photometric redshift estimation, for example, Gaussian process regression (Way & Srivastava, 2006; Way et al. 2009; Bonfield et al. 2010; Almosallam et al. 2016), kernel regression (Wang et al. 2007), Support Vector Machine (Jones & Singal 2017; Schindler et al. 2017; Jin et al. 2019), Random Forest (RF; Carliles et al. 2010; Schindler et al. 2017; Zhang et al. 2019; Zhou et al. 2021), artificial neural networks (Collister et al. 2007; Reis et al. 2012; Brescia et al. 2013; Amaro et al. 2019; Shuntov et al. 2020) and boosted decision trees (Gerdes et al. 2010), XGBOOST (Jin et al. 2019; Li et al. 2022), CATBOOST (Li et al. 2022), etc.

Moreover many works focused on the detailed comparison and application of different codes/algorithms. For instance, Sanchez et al. (2014) applied most of the existing photo- $z$  codes including some machine learning algorithms and template-fitting methods, to provide photometric redshifts of galaxies from the early data of the Dark Energy Survey. Beck et al. (2017) explored the performance of machine learning and template-fitting methods in the respect of redshift coverage, extrapolation and photometric errors, and provided the application reference on the choice of machine learning and template-fitting methods. Desprez et al. (2020) assessed the strengths and weaknesses of machine learning and template-fitting approaches, and found that a combination of both approaches with rejection criteria can outperform any individual method. Schmidt et al. (2020) compared 12 photo- $z$  algorithms, and indicated the influence of the assumptions underlying each technique on the performance of photometric redshift estimation.

Compared with machine learning methods, the template-fitting approach has three advantages: the first is that it does not require a sample set with known redshifts, the second is that it is not limited by the known sample redshift coverage and can be applied to larger redshifts, and the third is that it provides additional information to physically characterise the objects. For machine learning methods, better accuracy can be obtained in the redshift range of known samples, but the prediction range is also constrained by the redshifts of known samples. Combination of them is a good

choice. In this paper, we will employ two kinds of methods to carry out the redshift estimation of the DESI survey DR9 galaxies.

## 2 DATA

The Dark Energy Spectroscopic Instrument (DESI; DESI Collaboration, 2016a; DESI Collaboration, 2016b) Legacy Imaging Surveys (Dey et al. 2019) contain three optical telescopes to provide galaxy and quasar targets for follow-up observation by DESI. They survey the northern Galactic cap at  $\delta > 32^\circ$  and the South Galactic Cap region at  $\delta \leq 34^\circ$  in  $g, r, z$  bands, covering about  $14000 \text{ deg}^2$ , the Legacy Surveys deliver  $5\sigma$  detections of a “fiducial”  $g = 24.0$ ,  $r = 23.4$  and  $z = 22.5$  AB mag galaxy with an exponential light profile of half-light radius  $r_{\text{half}} = 0.45 \text{ arcsec}$ . The Data Release 9 (DR9) was released in 2021, which included images and catalogues. In this data release version, using the software package “TRACTOR” (Lang, Hogg & Mykytyn 2016), the forced photometries on  $W1$  and  $W2$  bands of the unWISE coadded images were obtained.

The spectroscopic data with redshifts are mainly from the Data Release 16 of the Sloan Digital Sky Survey (SDSS; York et al. 2000), the Data Release 7 of the Large Sky Area Multi-object Fiber Spectroscopic Telescope (LAMOST; Cui et al. 2012; Luo et al. 2015), the Data Release 3 of the Galaxy And Mass Assembly (GAMA; Baldry et al. 2018) and the WiggleZ Dark Energy Survey (WiggleZ; Parkinson et al. 2012). The cross-matched catalogue of SDSS DR16 (Lyke et al. 2020) and DESI DR9 has been released online <sup>1</sup>, which provides SDSS DR16 spectral information (MJD, PLATE, FIBERID). Then we cross match DESI DR9 with the SDSS DR16 galaxy catalogue with  $z_{\text{warning}} = 0$  to get spectral redshifts by the same MJD, PLATE and FIBERID. The cross-matched catalogue is called as the DSW sample. Then, we select galaxies with spectral redshifts  $z > 0$  and  $z_{\text{err}} \leq 0.01$  from the LAMOST DR7 galaxy catalogue, those with the redshift quality flag  $nQ = 4$  and  $z > 0$  from the GAMA DR3 catalogue, and those with the redshift quality flag  $Q \geq 4$  and  $z > 0$  from the WiggleZ catalogue, and then all these selected galaxies are respectively cross-matched to the DESI DR9 catalogue by positional cross-match with  $1.5 \text{ arcsec}$  radius. The nearest sources of all targets are kept, the obtained samples are defined as S\_LAMOST, S\_GAMA, S\_WiggleZ, respectively. After that, we compute the magnitudes corresponding to the model and aperture fluxes in  $g, r, z, W1, W2$  bands respectively, and remove the out-of-range sources with  $g > 24.0$ ,  $r > 23.4$ ,  $z > 22.5$ . We also delete all sources with  $\text{maskbits!} = 0$ , because these sources are either in corrupted imaging pixels, or pixels that in the vicinity of bright stars, globular clusters, or nearby galaxies. In this work, the DSW sample is used for training, validation and test, the other samples are applied for external test. The number of each sample is shown in Table 1.

All parameter information about the known samples is indicated in Table 2. The  $r$  magnitude distribution and

<sup>1</sup> [https://portal.nersc.gov/cfs/cosmo/data/legacysurvey/dr9/north\(south\)/external/](https://portal.nersc.gov/cfs/cosmo/data/legacysurvey/dr9/north(south)/external/)

**Table 1.** Number of objects from each spectroscopic survey that are cross-matched to DESI DR9.

Survey	Sample	No. of objects	Training, validation, test
SDSS	DSW	2 609 100	Training, validation, test
LAMOST	S_LAMOST	107 178	Test
GAMA	S_GAMA	126 254	Test
WiggleZ	S_WiggleZ	129 271	Test

the spectroscopic redshift distribution of the training and test samples are shown in Figure 1. As described in Figure 1, the distribution range of  $r$  magnitude for the external test samples (S\_LAMOST, S\_GAMA, S\_WiggleZ) is similar to that of the training sample DSW, and most sources from S\_LAMOST and S\_GAMA are bright while most from S\_WiggleZ are faint. The spectroscopic redshift range for the DSW sample and S\_WiggleZ is from 0 to 2, while that of S\_LAMOST and S\_GAMA is from 0 to 1.

### 3 METHOD

#### 3.1 EAZY approach

EAZY (Brammer et al. 2008) is a public photometric redshift code based on template-fitting algorithm, which combines features from various existing programs, such as the possibility of fitting linear combination of templates as done in GREGX (Ruknick et al. 2001; Ruknick et al. 2003), and a user-friendly interface based on HyperZ (Bolzonella et al. 2000). The basic algorithm of EAZY is to establish a redshift grid based on the SED templates, find the best-fitting template spectrum in each redshift grid, which minimizes the value of  $\chi^2$ , and no priors are needed.

$$\chi_{z,i}^2 = \sum_{j=1}^{N_{filt}} \frac{(T_{z,i,j} - F_j)^2}{(\delta F_j)^2} \quad (1)$$

where  $N_{filt}$  is the number of filters,  $T_{z,i,j}$  is the synthetic flux of template  $i$  in filter  $j$  for redshift  $z$ ,  $F_j$  is the observed flux in filter  $j$ , and  $\delta F_j$  is the uncertainty in  $F_j$ . Then, in EAZY, the linear combination of templates is implemented. In this improved algorithm, it finds the best-fitting coefficients  $\alpha$  of all combined templates, so that

$$T_z = \sum_{i=1}^{N_{temp}} \alpha_i T_{z,i} \quad (2)$$

This improvement is significant for accuracy, but more computation time is required. Meanwhile, for each estimation, EAZY calculates a parameter  $Q_z$  (see Equation 3), which demonstrates photometric redshift estimation quality. In general, the estimated redshift with  $Q_z < 1$  is considered as reliable.

$$Q_z = \frac{\chi^2}{N_{filter} - 3} \frac{z_{up}^{99} - z_{lo}^{99}}{p_{\Delta z=0.2}} \quad (3)$$

In Equation 3,  $\chi^2$ ,  $N_{filter}$  is the same as Equation 1,  $p_{\Delta z}$  represents the fraction of the total integrated probability that lies within  $\pm \Delta z$  of the estimated redshifts (Brammer et al. 2008).

Yang et al. (2014) estimated photometric redshifts of

the Hawaii-Hubble deep field-north(H-HDF-N) survey catalogue by EAZY. Chen et al. (2018) adopted EAZY to measure the redshifts of the XMM-Newton point source catalogue. The good performance is obtained in these researches. Thus, in this paper, we adopt EAZY as the representative of template-fitting method to predict the redshifts of DESI DR9 galaxies.

#### 3.2 CATBOOST

Gradient Boosted Decision Trees (GBDT, Friedman et al. 2001) are well fit for classification and regression tasks. CATBOOST (Dorogush et al. 2018), as a member of the family of GBDT, is a high-performance open source algorithm. CATBOOST applies boosting method to build strong classifiers or regressors by means of learning multiple weak classifiers or regressors. Comparing to GBDT, CATBOOST adopts Oblivious Decision Trees (ODT) to build decision trees, which are full binary trees, furthermore, all non-leaf nodes of ODT will have the same splitting criteria. This design is helpful to speed up the score and avoid over fitting. It has good characteristics of supporting categorical features and missing value in training data without additional pre-processing, which improves its usage efficiency. In addition, it achieves easily good performance with default model parameters.

Li et al. (2022) compared the photometric redshift performance of CATBOOST, XGBOOST (Chen & Guestrin, 2016), and Random Forest (RF; Breiman, 2001), and CATBOOST showed the best performance and the fastest training speed. Therefore, we adopt CATBOOST as the main machine learning method to predict redshifts of DESI DR9 galaxies. We perform all computation of this work provided by National Astronomical Data Centre (NADC) (Li et al. 2017).

### 4 PHOTOMETRIC REDSHIFT ESTIMATION

#### 4.1 Metrics

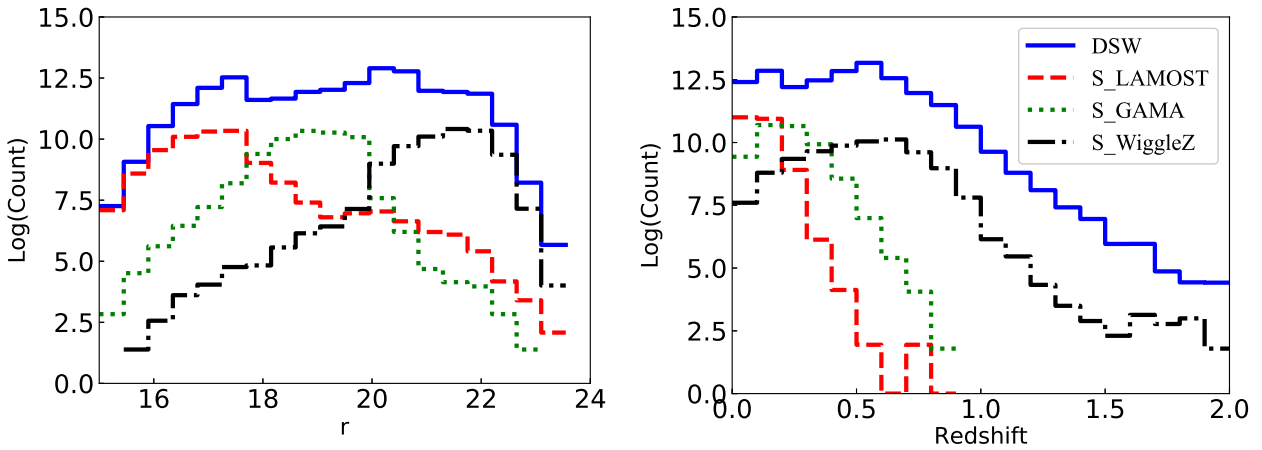
The performance of different algorithms on photometric redshift estimation may be judged by different metrics, for example, the residual between the spectroscopic and photometric redshifts,  $\Delta z = z_{spec} - z_{photo}$ , the mean absolute error (MAE) and the mean squared error (MSE). They are computed by the following equations:

$$MAE = \frac{1}{n} \sum_{i=0}^{n-1} |\Delta z| \quad (4)$$

$$MSE = \frac{1}{n} \sum_{i=0}^{n-1} (\Delta z)^2 \quad (5)$$

**Table 2.** Parameters in the known samples.

Parameter	Definition	Catalogue	Waveband
release	corresponds to the camera	DESI	
brickid	Brick ID	DESI	
objid	Source ID	DESI	
ra	Right ascension in decimal degrees	DESI	
dec	Declination in decimal degrees	DESI	
flux_g	Model flux in <i>g</i> band	DESI	Optical band
flux_r	Model flux in <i>r</i> band	DESI	Optical band
flux_z	Model flux in <i>z</i> band	DESI	Optical band
flux_w1	Model flux in <i>W1</i> band	DESI	Infrared band
flux_w2	Model flux in <i>W2</i> band	DESI	Infrared band
<i>g</i>	Model magnitude in <i>g</i> band	DESI	Optical band
<i>r</i>	Model magnitude in <i>r</i> band	DESI	Optical band
<i>z</i>	Model magnitude in <i>z</i> band	DESI	Optical band
<i>W1</i>	Model magnitude in <i>W1</i> band	DESI	Infrared band
<i>W2</i>	Model magnitude in <i>W2</i> band	DESI	Infrared band
flux_ivar_g	Inverse variance of flux_g	DESI	Optical band
flux_ivar_r	Inverse variance of flux_r	DESI	Optical band
flux_ivar_z	Inverse variance of flux_z	DESI	Optical band
flux_ivar_w1	Inverse variance of flux_w1	DESI	Optical band
flux_ivar_w2	Inverse variance of flux_w2	DESI	Optical band
apflux_g	Aperture fluxes in <i>g</i> band	DESI	Optical band
apflux_r	Aperture fluxes in <i>r</i> band	DESI	Optical band
apflux_z	Aperture fluxes in <i>z</i> band	DESI	Optical band
apflux_w1	Aperture fluxes in <i>w1</i> band	DESI	Infrared band
apflux_w2	Aperture fluxes in <i>w2</i> band	DESI	Infrared band
ap_g(1 ~ 8)	Aperture magnitude in <i>g</i> band	DESI	Optical band
ap_r(1 ~ 8)	Aperture magnitude in <i>r</i> band	DESI	Optical band
ap_z(1 ~ 8)	Aperture magnitude in <i>z</i> band	DESI	Optical band
ap_W1(1 ~ 5)	Aperture magnitude in <i>W1</i> band	DESI	Infrared band
ap_W2(1 ~ 5)	Aperture magnitude in <i>W2</i> band	DESI	Infrared band
z_spec	Spectral redshift	SDSS, LAMOST GAMA, WiggleZ	

**Figure 1.** Left panel: the number of galaxies as a function of *r* magnitude for the training (DSW) and test samples (S\_LAMOST, S\_GAMA, S\_WiggleZ); right panel: the number of galaxies as a function of spectroscopic redshifts for the training (DSW) and test samples (S\_LAMOST, S\_GAMA, S\_WiggleZ).

The fraction of test sample that satisfies  $|\Delta z| < e$  is usually used to evaluate the redshift estimation, where  $e$  is a given residual threshold (Schindler et al. 2017 and references therein). In general, the redshift normalized residuals

$\Delta z(\text{norm})$  are applied, and here  $e = 0.3$  is adopted.

$$\Delta z(\text{norm}) = \frac{z_{\text{spec}} - z_{\text{phot}}}{1 + z_{\text{spec}}} \quad (6)$$

$$\delta_{0.3} = \frac{N_{|\Delta z(\text{norm})| < 0.3}}{N_{\text{total}}} \quad (7)$$

Four additional metrics are defined as follows and used for performance evaluation of different machine learning methods: bias (the average separation between prediction and true values), the normalized standard deviation of the photometric redshifts and the spectroscopic redshifts, the normalized median absolute deviation ( $\sigma_{\text{NMAD}}$ ) and the outlier fraction ( $O$ ; Henghes et al. 2021; Curran et al. 2021).

$$\text{Bias} = \langle z_{\text{spec}} - z_{\text{phot}} \rangle \quad (8)$$

$$\sigma_{\Delta z(\text{norm})} = \sqrt{\frac{1}{n} \sum_{i=0}^{n-1} (\Delta z(\text{norm}) - \overline{\Delta z(\text{norm})})^2} \quad (9)$$

$$\sigma_{\text{NMAD}} = 1.48 \times \text{median} |\Delta z(\text{norm})| \quad (10)$$

$$\text{Outlier fraction}(O) = \frac{N_{|\Delta z(\text{norm})| > 0.15}}{N_{\text{total}}} \quad (11)$$

#### 4.2 Photometric redshift estimation by EAZY

We estimate photometric redshifts of all galaxies from training set by EAZY. For EAZY, the default v1.3 template set is adopted, which includes 9 templates. The parameter  $N_{\text{MIN\_COLORS}}$  is set to 4, which means that the number of filters with values is at least 4, and the other parameters are set as the default. Since each telescope has the respective filter response curves, the data in the south sky or north sky need to be estimated separately. Table 3 shows the performance of template-fitting approach for the south and north subsamples of the DSW sample, and Table 4 indicates the performance of template-fitting approach with  $Q_z < 1$ . The performance metrics are greatly improved, comparing the metrics in Table 4 with those in Table 3. If meeting the condition  $Q_z < 1$ , the estimated redshifts are more reliable. The scatter figure and  $\Delta z(\text{norm})$  distribution of estimated photometric redshifts and spectroscopic redshifts are indicated in Figure 2.

#### 4.3 Photometric redshift estimation by CATBOOST

Compared with template-fitting approach, the obvious characteristics of machine learning methods is that they need perform model training on known samples to establish a regressor for redshift estimation. The training process mainly includes feature selection, model parameter optimization and model validation.

##### 4.3.1 Feature selection

In machine learning algorithms, feature selection is the key step influencing the performance of photometric redshift estimation. According to the parameter description listed in Table 2, we choose features related to model magnitudes. These features include optical features  $g, r, z, g-r, r-z, g-z$ , and infrared related features  $W1, W2, g-W1, r-W1, z-W1, g-W2, r-W2, z-W2, W1-W2$ . Referring to the optimal feature selection procedure in Li et al. (2022),

we evaluate the importance score of each feature by CATBOOST, and sort them by the importance score. The importance score of each feature is shown in Figure 3. According to the rank of features, we select the top four features as initial input pattern to train, then add one feature in turn to the input pattern for training, and record all performance.  $MSE$ ,  $\sigma_{\text{NMAD}}$ , and  $O$  with different input features is described in Figure 4. Figure 4 indicates that  $MSE$ ,  $\sigma_{\text{NMAD}}$ , and  $O$  achieves the minimum when the number of input features is seven, and as the number of features increases, the performance fluctuates slightly. Therefore, the best input pattern (Pattern I, 7 features) is  $g-r, g, r-z, r, r-W1, z-W1, W1-W2$ , when only considering model magnitudes and colours.

Then, we mainly consider different aperture magnitudes as features. In the DESI DR9 catalogue, columns  $apflux_{\{g,r,z\}}$  contain eight different aperture fluxes in apertures of radius [0.5, 0.75, 1.0, 1.5, 2.0, 3.5, 5.0, 7.0] arc sec, and columns  $apflux_{w1}, apflux_{w2}$  contain five different aperture fluxes in apertures of radius [3, 5, 7, 9, 11] arc sec. We convert these fluxes to AB magnitudes. The similar feature importance procedure as the above is applied. The selected features contain  $g-ap_{g-1}, r-ap_{r-1}, z-ap_{z-1}, W1-ap_{W1-1}, W2-ap_{W2-1}$  and the difference between two adjacent aperture magnitudes (e.g.  $ap_{g-1} - ap_{g-2}, ap_{g-2} - ap_{g-3}, ap_{g-3} - ap_{g-4}, ap_{g-4} - ap_{g-5}, ap_{g-5} - ap_{g-6}, ap_{g-6} - ap_{g-7}, ap_{g-7} - ap_{g-8}$ ) and the colors for different apertures in two adjacent bands (e.g.  $ap_{g-1} - ap_{r-1}, ap_{r-1} - ap_{z-1}, ap_{z-1} - ap_{W1-1}, ap_{W1-1} - ap_{W2-1}$ ), which are ranked according to the importance score and regarded as Pattern II (60 features). If Pattern II is utilized, the best performance is  $MSE = 0.0056$ ,  $\sigma_{\text{NMAD}} = 0.0250$ . It is not better than the optimal model features (Pattern I).

Finally, combining the above obtained features related to model and aperture magnitudes, we obtain 75 features in total. We train again to get the importance score of each feature by CATBOOST and sort them. Those features with the score value of 0 are excluded. When 53 features are kept and defined as Pattern III, we get the best performance with  $MSE = 0.0034$  and  $\sigma_{\text{NMAD}} = 0.0173$  for this case. Table 5 shows that aperture information is helpful to improve the accuracy of photometric redshift estimation of galaxies. About the detailed definition of Patterns I, II and III refers to the Appendix.

Because galaxies are extended objects, they have different sizes based on their luminosity and distance, they usually seems bigger when they are bright and near. For a special galaxy, it has definitive size which corresponds to appropriate aperture, and aperture features influence physical parameter measurement of galaxies. Therefore we also consider aperture features as input for photo- $z$  estimation. Different types of galaxies have different shapes of spectral energy distribution (SED), and the SED shape of a galaxy will move to longer wavelength by a factor  $1+z$  at redshift  $z$ . The position of the obvious features (e.g. Lyman and Balmer breaks) as well as strong emission and absorption lines in a galaxy directly affects the shape of its low-resolution spectra, which in turn has effect on the photo- $z$  estimation. The flux becomes larger where emission line appears, while the flux turns smaller where absorption line emerges. For our sample, the redshift range is from 0 to 2. Taking Balmer breaks for example, the distribution of Balmer breaks is from 4000Å

**Table 3.** The performance of photometric redshift estimation with EAZY.

Subsample	MSE	MAE	<i>Bias</i>	$\sigma_{\text{NMAD}}$	$\sigma_{\Delta z(\text{norm})}$	$\delta_{0.3}(\%)$	$O(\%)$
DSW_south	0.0301	0.0719	-0.0217	0.0243	0.1128	98.79	5.12
DSW_north	0.0341	0.0621	0.0104	0.0224	0.1283	99.18	3.43

**Table 4.** The performance of photometric redshift estimation by EAZY when  $Q_z < 1$ .

Subsample	MSE	MAE	<i>Bias</i>	$\sigma_{\text{NMAD}}$	$\sigma_{\Delta z(\text{norm})}$	$\delta_{0.3}(\%)$	$O(\%)$	$Q_z > 1(\%)$
DSW_south	0.0088	0.0521	-0.0149	0.0219	0.0539	99.73	2.06	10.43
DSW_north	0.0085	0.0464	0.0044	0.0209	0.0574	99.83	1.77	6.56

to 12000Å, including  $g$ ,  $r$  and  $z$  band. As shown in Figure 1, most of our sample occupy at low redshift, so the features related to  $g$  and  $r$  show higher score, while those related to  $W2$  obtain lower score.

#### 4.3.2 Model parameter optimization

Model parameter optimization is a very complex and important task. CATBOOST is easy to achieve good performance with default parameters. Hence, we only choose the maximum depth of individual tree (*depth*) and the maximum number of trees (*iterations*) for optimization, for other parameters, the default values are adopted. For each training, we adopt 5-fold cross validation to obtain average *MSE*, *MAE*, *Bias*,  $\sigma_{\text{NMAD}}$ ,  $\sigma_{\Delta z(\text{norm})}$ ,  $\delta_{0.3}$ ,  $O$  and running time. There are two steps to find optimal *depth* and *iterations*. Firstly, we set *iterations* as 1000 (default value), and in turn *depth* is from 3 to 15. We separately perform this model parameter optimization procedure on the input patterns I and III. *MSE*,  $\sigma_{\text{NMAD}}$  and  $O$  of each training with different *depth* is displayed in Figure 5. Figure 5 shows that the performance with Pattern I reaches the best with  $MSE = 0.0037$  and  $O = 1.07$  per cent when *depth* = 8, the performance with Pattern III reaches the optimum with  $MSE = 0.0034$  and  $O = 0.92$  per cent when *depth* = 12. Secondly, we set *iterations* in [1000, 2000, 3000, 4000, 5000] in turn. For Pattern I, the optimal *iterations* is 4000 when *depth* = 8. For Pattern III, the optimal *iterations* is 5000 when *depth* = 12. The performance metrics with optimal model parameters are listed in Table 6. Table 6 suggests that the performance with Pattern III is superior to that with Pattern I.

Finally, we use the optimal pattern (Pattern III) and optimal model parameters (*depth* = 12 and *iterations* = 5000) of CATBOOST to train a regressor with the total sample, then use the same sample to evaluate. The performance is up to  $MSE = 0.0009$ ,  $MAE = 0.0182$ ,  $\sigma_{\text{NMAD}} = 0.0128$ ,  $\sigma_{\Delta z(\text{norm})} = 0.0199$ ,  $\delta_{0.3} = 99.98$  per cent, and  $O = 0.15$  per cent. The scatter figure and  $\Delta z(\text{norm})$  distribution of estimated photometric redshifts and spectroscopic redshifts are shown in Figure 6. Figure 6 implies that CATBOOST is reliable and efficient to estimate photometric redshifts of galaxies.

In order to assess the performance with magnitude and redshift for CATBOOST, Figure 7 depicts the metrics (*MSE*,  $\sigma_{\text{NMAD}}$ ,  $O$ ) as a function of  $r$  magnitude and redshift for the whole DSW sample, respectively. It shows that the three metrics become larger with the increase of magnitude, in other words, the performance of photometric redshift esti-

mation declines when the celestial objects get fainter. It also indicates that the three metrics wave with different redshifts, and rise when redshift is larger than about 0.6, that is to say, the performance of the regressor is influenced by redshifts and decreases at higher redshift.

#### 4.3.3 Model Test

After the CATBOOST regressor is established, we use three external test samples (S\_LAMOST, S\_GAMA, S\_WiggleZ) to test the performance of this regressor. The performance metrics for the test samples are described in Table 7. The scatter of photometric redshifts vs. spectroscopic redshifts are displayed respectively in Figure 8. Table 7 and Figure 8 show the estimation accuracy of photometric redshifts for different test samples is different, obviously the prediction accuracy with the S\_LAMOST and S\_GAMA samples are better than that with the S\_WiggleZ sample. It further proves that the prediction accuracy is affected by the magnitude and redshifts of samples. The sources with brighter magnitude and lower redshift have better prediction accuracy, which is consistent with the fact that most of the S\_LAMOST and S\_GAMA samples are brighter and at lower redshifts while most of the S\_WiggleZ sample are fainter. For the S\_WiggleZ sample, the performance as a function of magnitude and redshift is shown in Figure 9. Comparing Figure 9 to Figure 7, the trends with magnitude are almost similar but the trend with magnitude in Figure 9 is higher than in Figure 7; the trends with redshift are clearly different; when redshift is larger than 0.6 the trends with redshift both become gradual. This result may be due to the selection effect that the S\_WiggleZ sample is inclined to emission galaxies.

## 4.4 Comparison and discussion

Although CATBOOST is optimal compared to XGBoost and Random Forest (RF) in Li et al. (2022), the performance is closely related to used samples. We adopt multi-layer perceptron (MLP) and RF to train regressors again with Pattern III respectively. The python code packages of MLP and RF are provided by scikit-learn (Pedregosa et al. 2011). Table 8 shows their optimal performance. Comparing the results of different methods in Table 8, it is found that the performance of CATBOOST is superior to that of MLP in respect of all metrics, CATBOOST outperforms RF except Bias, moreover CATBOOST has much shorter training time than RF.

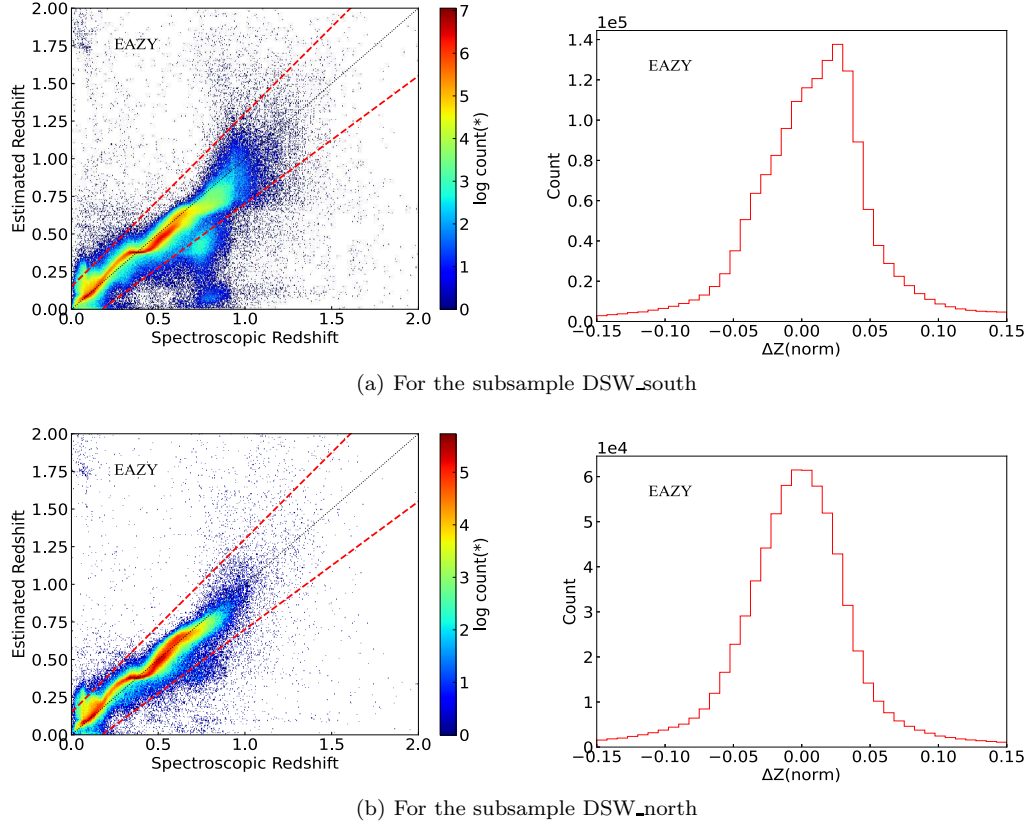


**Figure 2.** The scatter figure and  $\Delta z(\text{norm})$  distribution of estimated photometric redshifts and spectroscopic redshifts for the subsamples of the DSW sample by EAZY. In the scatter figure, the red dashed line represents  $\Delta z(\text{norm}) = \pm 0.3$  separately.

**Table 5.** The performance of photometric redshift estimation by CATBOOST with default model parameters.

Sample	Pattern	MSE	MAE	Bias	$\sigma_{\text{NMAD}}$	$\sigma_{\Delta z(\text{norm})}$	$\delta_{0.3}(\%)$	$O(\%)$	Time(s)
DSW	Pattern I	0.0038	0.0304	$1.0 \times 10^{-6}$	0.0180	0.0406	99.72	1.08	88
DSW	Pattern II	0.0056	0.0412	$2.85 \times 10^{-4}$	0.0250	0.0504	99.64	2	154
DSW	Pattern III	0.0034	0.0291	$3.6 \times 10^4$	0.0173	0.0384	99.76	0.95	143

<sup>a</sup> Pattern I represents  $g - r, g, r - z, r, r - W1, z - W1, W1 - W2$  (7 features).

<sup>b</sup> Pattern II (60 features) and Pattern III (53 features) are described in the APPENDIX.

**Table 6.** The performance of photometric redshift estimation with the best features and optimal model parameters by CATBOOST.

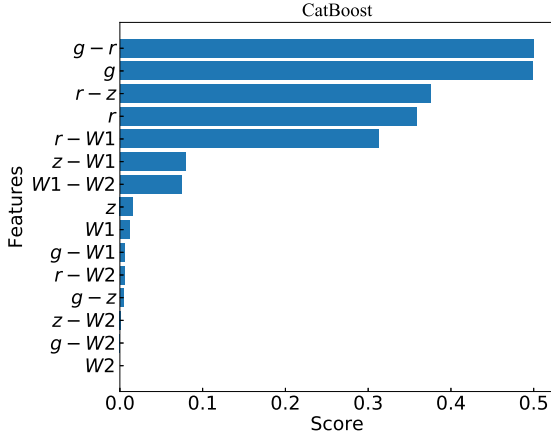
Sample	Pattern	Model parameter	MSE	MAE	Bias	$\sigma_{\text{NMAD}}$	$\sigma_{\Delta z(\text{norm})}$	$\delta_{0.3}(\%)$	$O(\%)$	Time(s)
DSW	Pattern I	$\text{depth} = 8$ $\text{iterations} = 4000$	0.0037	0.0299	$4.8 \times 10^{-5}$	0.0175	0.0405	99.72	1.06	381
DSW	Pattern III	$\text{depth} = 12$ $\text{iterations} = 5000$	0.0032	0.0272	$3.3 \times 10^{-4}$	0.0156	0.0371	99.76	0.88	3484

**Table 7.** The performance of the external test samples.

Test Sample	MSE	MAE	Bias	$\sigma_{\text{NMAD}}$	$\sigma_{\Delta z(\text{norm})}$	$\delta_{0.3}(\%)$	$O(\%)$
S_LAMOST	0.0010	0.0142	0.0022	0.0113	0.0242	99.86	0.49
S_GAMA	0.0022	0.0273	0.0015	0.0202	0.0351	99.62	1.06
S_WiggleZ	0.0208	0.0981	-0.031	0.0669	0.0661	99.03	9.04

**Table 8.** The performance of photometric redshift estimation with the best features and optimal model parameters by different methods.

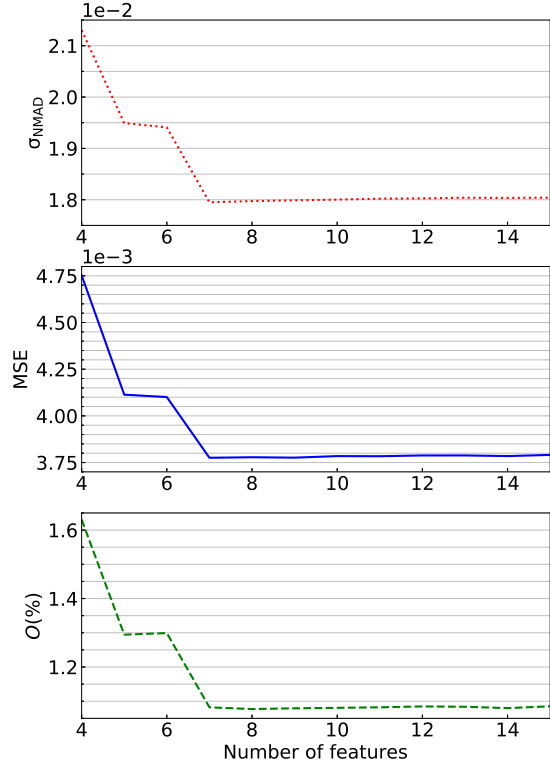
Sample	Method	Pattern	Model parameter	MSE	MAE	Bias	$\sigma_{\text{NMAD}}$	$\sigma_{\Delta z(\text{norm})}$	$\delta_{0.3}(\%)$	$O(\%)$	Time(s)
DSW	CATBOOST	Pattern III	$depth = 12$ $iterations = 5000$	0.0032	0.0272	$3.3 \times 10^{-4}$	0.0156	0.0371	99.76	0.88	3484
DSW	MLP	Pattern III	$hidden\_layer\_sizes = 100$ $max\_iter = 200$	0.0044	0.0367	$1.1 \times 10^{-3}$	0.0246	0.0439	99.71	1.38	464
DSW	RF	Pattern III	$max\_depth = 12$ $n\_estimators = 300$	0.0037	0.0306	$1.9 \times 10^{-4}$	0.0183	0.0401	99.74	1.04	34044

**Figure 3.** The feature importance for the DSW sample by CATBOOST.

Zhou et al. (2021) explored the clustering of DESI-like luminous red galaxies by photometric redshifts and adopted Random Forest method to estimate photometric redshifts of DESI DR8. Comparing our work with Zhou et al. (2021), the differences are methods and data, as shown in Table 9. Tables 8-9 both further suggests that CATBOOST outperforms Random Forest for our case. Zhou et al. (2021) presented photometric redshifts for DESI DR8 with Random Forest while we provide the photometric redshift measurement for DESI DR9 by means of CATBOOST and EAZY.

#### 4.5 Application

Based on the above experimental results for the known samples, we use EAZY and CATBOOST to predict photometric redshifts of galaxies from DESI DR9. We select all galaxy sources whose morphological classification types are equal to 'REX', 'EXP', 'DEV' or 'SER'. The number of sources amounts to 1 160 568 989. We estimate photometric redshifts of these galaxies using EAZY and CATBOOST with optimized parameters, respectively. EAZY can predict redshifts of galaxies ranging from 0 to 6. Table 10 lists the number of predicted DESI DR9 galaxies with  $maskbits = 0$  and  $Q_z < 1$  in different redshift ranges by EAZY. As shown in Table 10, the number of galaxies with predicted redshifts above 2 occupies about 6 per cent. For predicted DESI DR9 galaxies with  $maskbits = 0$ ,  $g \leq 24.0$ ,  $r \leq 23.4$  and  $z \leq 22.5$ , the predicted results by CATBOOST are more reliable when estimated redshifts is below 2, those by EAZY are more confident when estimated redshifts is greater than 2 and  $Q_z < 1$ . As a re-

**Figure 4.** MSE,  $\sigma_{\text{NMAD}}$ , and  $O$  as a function of different features by CATBOOST.

sult, EAZY is very useful for finding high redshift galaxies. While for the out-of-range sources with  $g > 24.0$ ,  $r > 23.4$  or  $z > 22.5$ , the predicted redshifts are only for reference. The whole predicted results by EAZY and CATBOOST are saved in 1107 files, which is of great value for the further study on the characteristics and evolution of galaxies. The result file link address is <https://doi.org/10.12149/101162>. For simplicity, Table 11 only lists 20 rows of predicted results, but all column of fluxes and magnitudes related are saved in the result files.

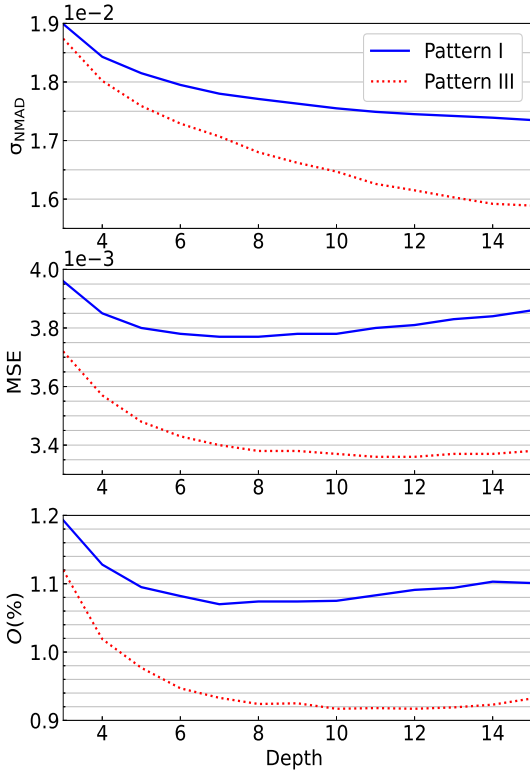
**Table 9.** Comparison of photometric redshift estimation in our work with that in Zhou et al. (2021).

Work	Data	Method	$\sigma_{\text{NMAD}}$	$O(0.10)(\%)$
Zhou et al. (2021)	DESI DR8 South ( $MAG\_Z \leq 21$ )	RF	0.0133	1.51
Our work	DESI DR8 North ( $MAG\_Z \leq 21$ )	RF	0.0136	0.92
	DESI DR8 South ( $MAG\_Z > 21$ )	RF	0.0725	24.6
	DESI DR9 South ( $MAG\_Z \leq 21$ )	CATBOOST	0.0126	0.34
	DESI DR9 North ( $MAG\_Z \leq 21$ )	CATBOOST	0.0130	0.22
	DESI DR9 South ( $MAG\_Z > 21$ )	CATBOOST	0.0148	1.24
	DESI DR9 North ( $MAG\_Z > 21$ )	CATBOOST	0.0132	1.39

<sup>a</sup>  $O(0.10)$  represents outlier fraction of  $|\Delta z(\text{norm})| > 0.10$ .

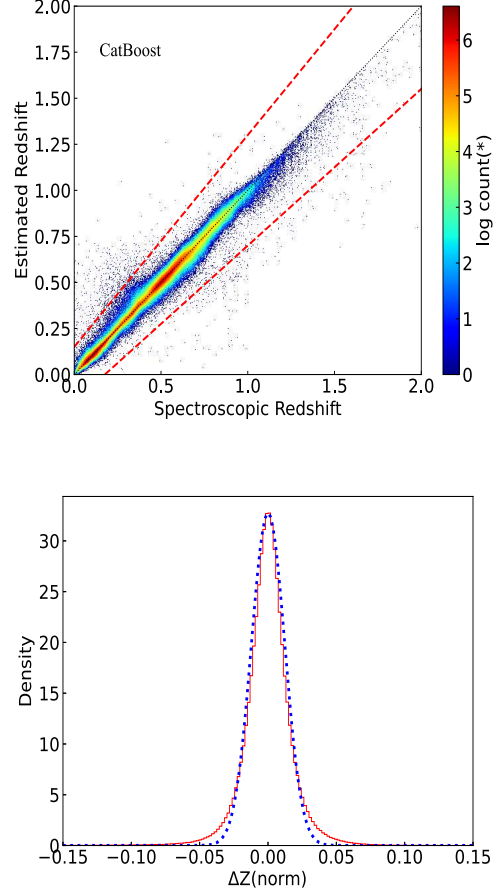
**Table 10.** The number of predicted DESI DR9 galaxies with  $\text{maskbits} = 0$  and  $Q_z < 1$  in different redshift ranges by EAZY.

Method	$0 < \text{redshift} < 2$	$2 \leq \text{redshift} < 3.5$	$3.5 \leq \text{redshift} < 4.5$	$4.5 \leq \text{redshift} < 5.5$	$\text{redshift} \geq 5.5$
EAZY	348 853 174	15 826 023	3 328 406	1 635 656	127 971

**Figure 5.** MSE,  $\sigma_{\text{NMAD}}$  and O by CATBOOST with different depth.

## 5 CONCLUSIONS

We adopt template fitting and machine learning to predict photometric redshifts of galaxies. We discuss the advantages and disadvantages of both approaches. Template fitting methods are not affected by known samples and can predict galaxies with higher redshifts, while machine learning methods can achieve higher accuracy through model train-

**Figure 6.** The evaluation performance of photometric redshift estimation with CATBOOST. In the scatter figure of photometric redshifts vs. spectroscopic redshifts, the red dashed line represents  $\Delta z(\text{norm}) = \pm 0.3$  separately. The distribution of  $\Delta z(\text{norm})$  is between -0.15 and 0.15, the blue dotted curve is the best-fitting normal distribution.

ing, but due to the lack of high redshift galaxies in currently known samples, the high redshift galaxies will be predicted to be low redshift ones. For low redshift galaxies (redshift  $z < 2$  for our case), CATBOOST is a good choice to estimate

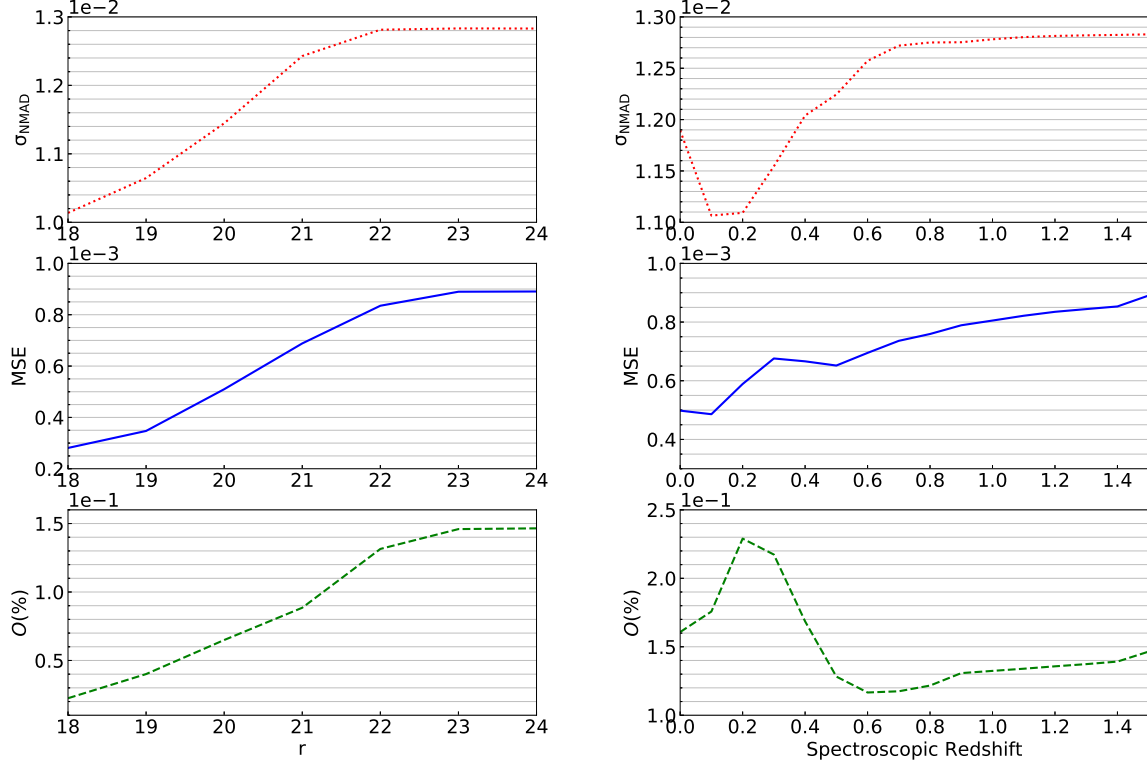
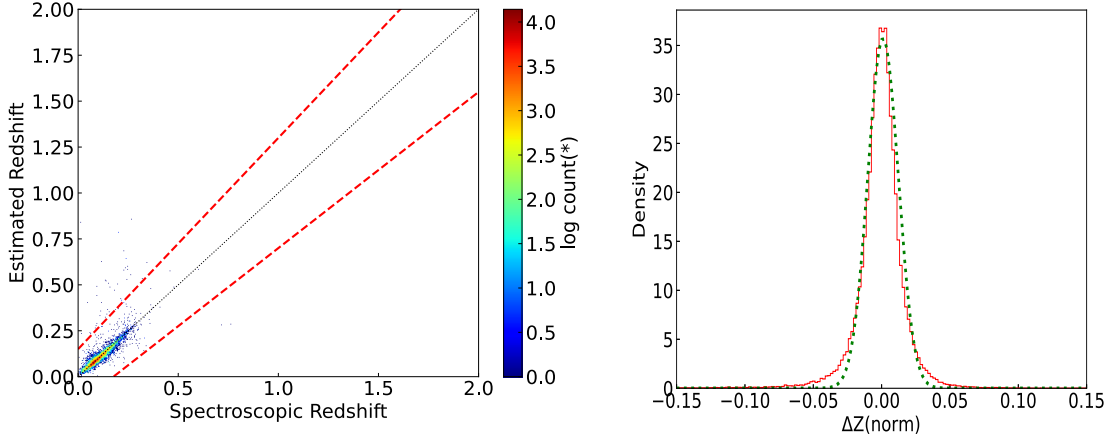


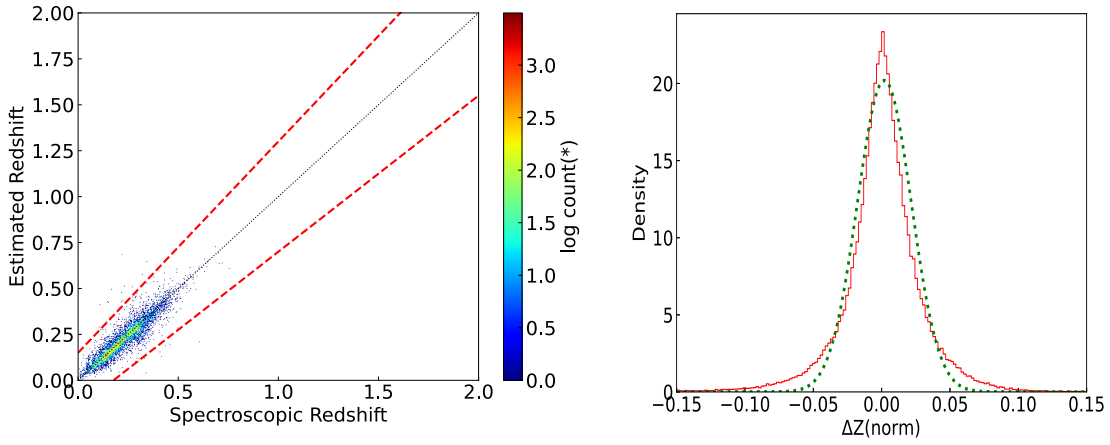
**Figure 7.** Left panel: the  $\sigma_{\text{NMAD}}$ ,  $\text{MSE}$ ,  $O$  as a function of  $r$  magnitude for the whole DSF sample. Right panel: the  $\sigma_{\text{NMAD}}$ ,  $\text{MSE}$ ,  $O$  as a function of spectroscopic redshifts for the whole DSF sample.

**Table 11.** The estimated photometric redshifts of DESI DR9 galaxies,  $z_{\text{cb}}$  is predicted redshift by CATBOOST,  $z_{\text{eazy}}$  is predicted redshift by EAZY,  $Q_z$  demonstrates photometric redshift estimation quality of EAZY,  $n_{\text{filt}}$  is the number of used filters.

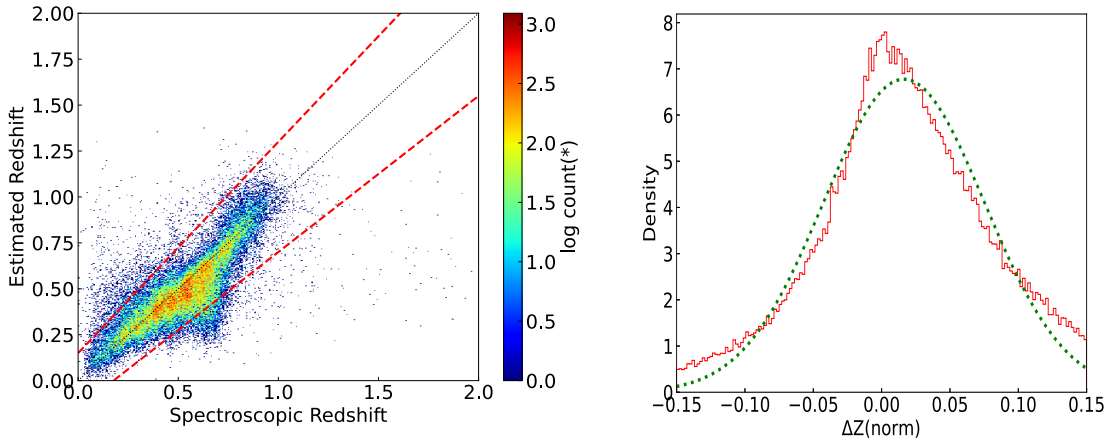
release	brickid	objid	RA	Dec	$z_{\text{cb}}$	$z_{\text{eazy}}$	$Q_z$	$n_{\text{filt}}$
9010	465328	3933	140.60547174695245	23.89775480146321	0.447	0.277	5.420	5
9010	465328	3935	140.60570892573824	23.913236038787858	0.980	1.395	8.351	5
9010	465328	3936	140.60576126216455	24.08768860870403	0.520	0.375	0.047	4
9010	465328	3937	140.60576728408122	24.075655633141213	0.949	1.206	3.747	5
9010	465328	3938	140.60577110445337	24.033382424270663	0.871	1.142	4.221	4
9010	465328	3940	140.60592807141936	23.998381611411066	0.650	1.125	56.022	4
9010	465328	3942	140.60615861124148	23.94613561864017	0.969	1.677	13.574	5
9010	465328	3944	140.60620883781942	23.912058728862267	0.889	0.932	2.866	5
9010	465328	3948	140.60638882279335	24.028406631122056	1.140	1.305	1.543	5
9010	465328	3949	140.60641713623545	23.87420843970829	0.913	1.804	0.011	5
9010	465328	3954	140.60659960507638	23.910351365034238	0.844	0.500	0.333	5
9010	465328	3955	140.60663973978004	24.007290234431604	0.858	0.850	1.715	5
9010	465328	3956	140.60683707462877	24.04563942636601	0.738	0.711	1.145	4
9010	465328	3957	140.6068563283938	24.110469165376028	0.824	0.884	1.728	5
9010	465328	3958	140.60685843145077	24.106992421044172	0.468	2.298	3.353	4
9010	465328	3960	140.6068938439817	24.117431904938048	0.503	1.766	39.261	4
9010	465328	3964	140.60719039910862	24.04818401589685	0.605	0.320	0.889	4
9010	465328	3965	140.60724459654958	24.057913639613552	0.953	1.741	0.882	4
9010	465328	3967	140.6073643677021	24.03165350182948	0.246	0.297	5.305	4
9010	465328	3968	140.60753251569648	24.066669913889974	0.483	2.658	10.795	5



(a) For the LAMOST sample.



(b) For the GAMA sample.



(c) For the WiggleZ sample.

**Figure 8.** Photometric redshift estimation with the external test samples S\_LAMOST, S\_GAMA, S\_WiggleZ. In the scatter figure of photometric redshifts vs. spectroscopic redshifts, the red dashed line represents  $\Delta z(\text{norm}) = \pm 0.3$  separately. For the  $\Delta z(\text{norm})$  distribution, red line for the  $\Delta z(\text{norm})$  distribution and green dotted line is the best-fitting normal distribution.

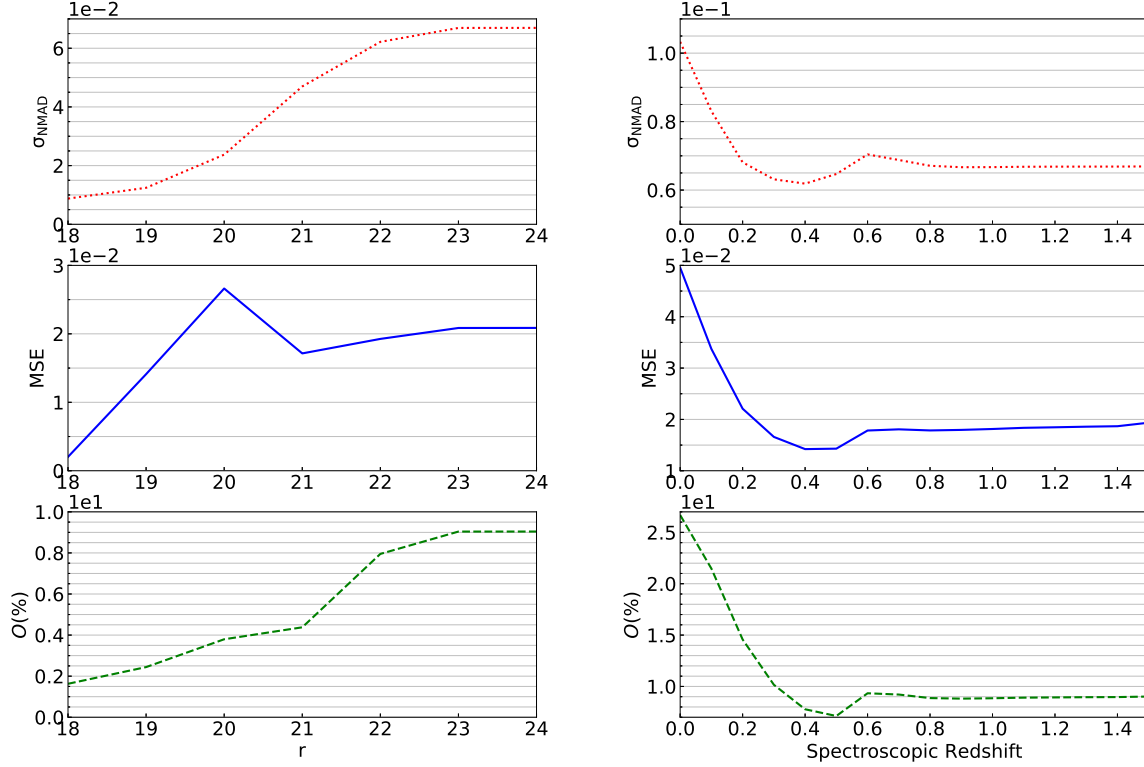


**Figure 9.** Left panel: the  $\sigma_{\text{NMAD}}$ ,  $MSE$ ,  $O$  as a function of  $r$  magnitude for the WiggleZ sample. Right panel: the  $\sigma_{\text{NMAD}}$ ,  $MSE$ ,  $O$  as a function of spectroscopic redshifts for the WiggleZ sample.

their photometric redshifts; for high redshift ones, EAZY is more appropriate. Thus, we utilize the two methods to predict photometric redshifts of all galaxies from DESI Legacy Imaging Surveys DR9. The estimated photometric redshifts of galaxies will be very valuable for future research, and can help spectroscopic sky survey projects (e.g. SDSS, DESI) for follow up observation to spot more high redshift galaxies.

## 6 ACKNOWLEDGEMENTS

We are very grateful to the referee’s constructive suggestions. This work is supported by National Natural Science Foundation of China (NSFC)(grant Nos. 11803055, 12273076, 12103070, 11573019, 11873066, 12133001, 11433005), the Joint Research Fund in Astronomy (U1931132, U1531246, U1731125, U1731243, U1731109) under cooperative agreement between the NSFC and Chinese Academy of Sciences (CAS), the 14th Five-year Informatization Plan of Chinese Academy of Sciences (CAS-WX2021SF-0204) and the science research grants from the China Manned Space Project with Nos. CMS-CSST-2021-A04 and CMS-CSST-2021-A06. Data resources are supported by Chinese Astronomical Data Center (NADC), CAS Astronomical Data Center and Chinese Virtual Observatory (China-VO). This work is supported by Astronomical Big Data Joint Research Center, co-founded

by National Astronomical Observatories, Chinese Academy of Sciences and Alibaba Cloud.

The Guoshoujing Telescope (the Large Sky Area Multi-object Fiber Spectroscopic Telescope, LAMOST) is a National Major Scientific Project built by the Chinese Academy of Sciences. Funding for the project has been provided by the National Development and Reform Commission. LAMOST is operated and managed by the National Astronomical Observatories, Chinese Academy of Sciences.

The Legacy Surveys consist of three individual and complementary projects: the Dark Energy Camera Legacy Survey (DECaLS; Proposal ID #2014B-0404; PIs: David Schlegel and Arjun Dey), the Beijing-Arizona Sky Survey (BASS; NOAO Prop. ID #2015A-0801; PIs: Zhou Xu and Xiaohui Fan), and the Mayall z-band Legacy Survey (MzLS; Prop. ID #2016A-0453; PI: Arjun Dey). DECaLS, BASS and MzLS together include data obtained, respectively, at the Blanco telescope, Cerro Tololo Inter-American Observatory, NSF’s NOIRLab; the Bok telescope, Steward Observatory, University of Arizona; and the Mayall telescope, Kitt Peak National Observatory, NOIR Lab. The Legacy Surveys project is honored to be permitted to conduct astronomical research on Iolkam Du’ag (Kitt Peak), a mountain with particular significance to the Tohono O’odham Nation.

NOIRLab is operated by the Association of Universities

for Research in Astronomy (AURA) under a cooperative agreement with the National Science Foundation.

This project used data obtained with the Dark Energy Camera (DECam), which was constructed by the Dark Energy Survey (DES) collaboration. Funding for the DES Projects has been provided by the U.S. Department of Energy, the U.S. National Science Foundation, the Ministry of Science and Education of Spain, the Science and Technology Facilities Council of the United Kingdom, the Higher Education Funding Council for England, the National Center for Supercomputing Applications at the University of Illinois at Urbana-Champaign, the Kavli Institute of Cosmological Physics at the University of Chicago, Center for Cosmology and Astro-Particle Physics at the Ohio State University, the Mitchell Institute for Fundamental Physics and Astronomy at Texas A&M University, Financiadora de Estudos e Projetos, Fundacao Carlos Chagas Filho de Amparo, Financiadora de Estudos e Projetos, Fundacao Carlos Chagas Filho de Amparo a Pesquisa do Estado do Rio de Janeiro, Conselho Nacional de Desenvolvimento Cientifico e Tecnológico and the Ministerio da Ciencia, Tecnologia e Inovacao, the Deutsche Forschungsgemeinschaft and the Collaborating Institutions in the Dark Energy Survey. The Collaborating Institutions are Argonne National Laboratory, the University of California at Santa Cruz, the University of Cambridge, Centro de Investigaciones Energeticas, Medioambientales y Tecnologicas-Madrid, the University of Chicago, University College London, the DES-Brazil Consortium, the University of Edinburgh, the Eidgenössische Technische Hochschule (ETH) Zurich, Fermi National Accelerator Laboratory, the University of Illinois at Urbana-Champaign, the Institut de Ciències de l'Espai (IEEC/CSIC), the Institut de Física d'Altes Energies, Lawrence Berkeley National Laboratory, the Ludwig Maximilians Universität München and the associated Excellence Cluster Universe, the University of Michigan, NSF's NOIRLab, the University of Nottingham, the Ohio State University, the University of Pennsylvania, the University of Portsmouth, SLAC National Accelerator Laboratory, Stanford University, the University of Sussex, and Texas A&M University.

BASS is a key project of the Telescope Access Program (TAP), which has been funded by the National Astronomical Observatories of China, the Chinese Academy of Sciences (the Strategic Priority Research Program "The Emergence of Cosmological Structures" Grant # XDB09000000), and the Special Fund for Astronomy from the Ministry of Finance. The BASS is also supported by the External Cooperation Program of Chinese Academy of Sciences (Grant # 114A11KYSB20160057), and Chinese National Natural Science Foundation (Grant # 11433005).

The Legacy Survey team makes use of data products from the Near-Earth Object Wide-field Infrared Survey Explorer (NEOWISE), which is a project of the Jet Propulsion Laboratory/California Institute of Technology. NEOWISE is funded by the National Aeronautics and Space Administration.

The Legacy Surveys imaging of the DESI footprint is supported by the Director, Office of Science, Office of High Energy Physics of the U.S. Department of Energy under Contract No. DE-AC02-05CH1123, by the National Energy Research Scientific Computing Center, a DOE Office of Science User Facility under the same contract; and by the U.S.

National Science Foundation, Division of Astronomical Sciences under Contract No. AST-0950945 to NOAO.

We acknowledge SDSS databases. Funding for the Sloan Digital Sky Survey IV has been provided by the Alfred P. Sloan Foundation, the U.S. Department of Energy Office of Science, and the Participating Institutions. SDSS-IV acknowledges support and resources from the Center for High-Performance Computing at the University of Utah. The SDSS web site is [www.sdss.org](http://www.sdss.org). SDSS-IV is managed by the Astrophysical Research Consortium for the Participating Institutions of the SDSS Collaboration including the Brazilian Participation Group, the Carnegie Institution for Science, Carnegie Mellon University, the Chilean Participation Group, the French Participation Group, Harvard-Smithsonian Center for Astrophysics, Instituto de Astrofísica de Canarias, The Johns Hopkins University, Kavli Institute for the Physics and Mathematics of the Universe (IPMU) /University of Tokyo, Lawrence Berkeley National Laboratory, Leibniz Institut für Astrophysik Potsdam (AIP), Max-Planck-Institut für Astronomie (MPIA Heidelberg), Max-Planck-Institut für Astrophysik (MPA Garching), Max-Planck-Institut für Extraterrestrische Physik (MPE), National Astronomical Observatories of China, New Mexico State University, New York University, University of Notre Dame, Observatório Nacional / MCTI, The Ohio State University, Pennsylvania State University, Shanghai Astronomical Observatory, United Kingdom Participation Group, Universidad Nacional Autónoma de México, University of Arizona, University of Colorado Boulder, University of Oxford, University of Portsmouth, University of Utah, University of Virginia, University of Washington, University of Wisconsin, Vanderbilt University, and Yale University.

## 7 DATA AVAILABILITY

The predicted photometric redshifts for DESI DR9 galaxies are saved in a repository and can be obtained by a unique identifier, part of which is indicated in Table 11. It is put in paperdata repository of NADC at <http://paperdata.china-vo.org>, and can be available with <https://doi.org/10.12149/101162>.

## REFERENCES

- Almosallam I. A., Lindsay S. N., Jarvis M. J., Roberts, S. J., 2016, MNRAS, 455, 2387
- Amaro V. et al., 2019, MNRAS, 482, 3116
- Arnouts S., Cristiani S., Moscardini L., Matarrese S. Lucchin F. Fontana A. Giallongo E., 1999, MNRAS, 310, 540
- Babbedge T. S. R. et al., 2004, MNRAS, 353, 654
- Baldry I. K. et al., 2018, MNRAS, 474, 3875
- Beck R. et al., 2017, MNRAS, 468, 4323
- Bender R. et al., 2001, Deep Fields: Proceedings of the ESO Astrophysics symposia held at Garching, Germany, 9-12 Oct. 2000, Edited by S. Cristiani, A. Renzini, and R. E. Williams. Springer-Verlag, 2001, p.96
- Benitez N., 2000, ApJ, 536(2), 571

- Bonfield D. G., Sun Y., Davey N., Jarvis M. J., Abdalla F. B., Banerji M., Adams R. G., 2010, MNRAS, 405(2), 987
- Bolzonello M., et al., 2000, A&A, 363, 476
- Brammer G. B., Van Dokkum P. G., Coppi P., 2008, ApJ, 686, 1503
- Breiman L., 2001, Machine Learning, 45, 5
- Brescia M., Cavuoti S., D’Abrusco R., Longo G., Mercurio A., 2013, ApJ, 772(2), article id: 140, 12 pp.
- Carlles S., Budavári T., Heinis S., Priebe C., Szalay A. S., 2010, ApJ, 712(1), 511
- Chambers K. et al., 2016, e-prints arXiv: 1612.05560
- Chen T., Guestrin C., 2016, Proceedings of the 22nd ACM SIGKDD International Conference on Knowledge Discovery and Data Mining. ACM
- Connolly A. J., Csabai I., Szalay A. S., Koo D. C., Kron R. G., Munn J. A., 1995, AJ, 110, 2655
- Collister A. et al., 2007, MNRAS, 375, 68
- Csabai I. et al. 2003, AJ, 119, 69
- Chen C.-T. J. et al., 2018, MNRAS, 478, 2132
- Cui X.-Q. et al., 2012, RAA, 12, 1197
- Curran S. J., Moss J. P., Perrott Y. C., 2021, MNRAS, 503, 2639
- de Jong J. T. A. et al. 2013, The Messenger, 154, 44
- The Dark Energy Survey Collaboration, 2005, e-prints arXiv: astro-ph/0510346
- DESI Collaboration, 2016a, e-prints arXiv: 1611.00037
- DESI Collaboration, 2016b, e-prints arXiv: 1611.00036
- Desprez G. et al., 2020, A&A, 644, A31
- Dey A. et al., 2019, AJ, 157(5), article id: 168
- Dorogush A. V., Ershov V., Yandex A. G., 2018, e-prints arXiv:1810.11363
- Feldmann R. et al., 2006, MNRAS, 372, 565
- Friedman J. H., 2001, Annals of statistics, 29, 1189
- Gerdes D. W., Sypniewski, A. J., McKay, T. A., Hao, Jiang-gang, Weis, M. R., Wechsler, R. H., Busha, M. T., 2010, AJ, 715(2), 823
- Henghes B., Pettitt C., Thiyaalingam J., Hey T., Lahav O., 2021, MNRAS, 505, 4847
- Jin X., Zhang Y., Zhang J., Zhao Y., Wu X., Fan, D., 2019, MNRAS, 485, 4539
- Jones E., Singal J., 2017, A&A, 600, id.A113, 11 pp
- Lang D., Hogg D. W., Mykytyn D., 2016, Astrophysics Source Code Library, record ascl:1604.008
- Le Borgne D., Rocca-Volmerange B., 2002, A&A, 386, 446
- Li C. et al., 2017, Astrominformatics, Proceedings of the International Astronomical Union, IAU Symposium, 325, 353
- Li C. et al., 2022, MNRAS, 509, 2289
- Luo A. L. et al., 2015, RAA, 15, 1095
- Lyke B. W. et al. 2020, ApJS, 250, 8
- Nishizawa, A. J., Hsieh, B. C., Tanaka, M., Takata, T., 2020, e-prints arXiv: 2003.01511
- Parkinson D. et al., 2012, Phys. Rev. D, 86
- Puschell J., Owen F., Laing R. 1982, Proceedings of the International Astronomical Union, IAU Symposium, 97, 423
- Pedregosa F. et al., 2011, Journal of Machine Learning Research, 12, 2825
- Reis R. R. R. et al., 2012, ApJ, 747, 59
- Rudnick G., et al., 2001, AJ, 122, 2205
- Rudnick G., et al., 2003, ApJS, 172, 117
- Sánchez C., et al. 2014, MNRAS, 445(2), 1482
- Schmidt S. J., et al. 2020, MNRAS, 499, 1587
- Schindler J., Fan X., McGreer I. D., Yang Q., Wu J., Jiang L., Green R., 2017, ApJ, 851, 13
- Shuntov M., Pasquet J., Arnouts S., et al., 2020, A&A, 636, A90
- Wang D., Zhang Y., Liu C., Zhao Y., 2007, MNRAS, 382(4), 1601
- Way M. J., Srivastava A. N., 2006, ApJ, 647(1), 102
- Way M. J., Foster L. V., Gazis P. R., Srivastava A. N., 2009, ApJ, 706(1), 623
- York D. G. et al., 2000, AJ, 120, 1579
- Yang G. et al., 2014, ApJS, 215, 27
- Zhang Y., Ma H., Peng N., Zhao Y., Wu X.-b., 2013, AJ, 146(2), article id. 22, 10pp
- Zhang Y.-X., Zhang J.-Y., Jin X., Zhao Y.-H., 2019, RAA, 19, 169
- Zhou R. et al., 2021, MNRAS, 501, 3309
- Zou H. et al., 2022, RAA, 22, 065001

## 8 APPENDIX: PATTERN DEFINITION

The patterns used in this paper is defined as follows:

Pattern I represents  $g-r$ ,  $g$ ,  $r-z$ ,  $r$ ,  $r-W1$ ,  $z-W1$ ,  $W1-W2$  (7 features).

Pattern II is  $ap\_r4-ap\_z4$ ,  $ap\_g5-ap\_R5$ ,  $z-ap\_z1$ ,  $ap\_r6-ap\_z6$ ,  $g-ap\_g1$ ,  $ap\_z4-ap\_z5$ ,  $r-ap\_r1$ ,  $ap\_z1-ap\_z2$ ,  $ap\_r1-ap\_r2$ ,  $ap\_r4-ap\_r5$ ,  $ap\_g6-ap\_r6$ ,  $ap\_r7-ap\_z7$ ,  $ap\_z2-ap\_z3$ ,  $ap\_r5-ap\_z5$ ,  $ap\_r8-ap\_z8$ ,  $ap\_g4-ap\_g5$ ,  $ap\_z3-ap\_z4$ ,  $ap\_r2-ap\_r3$ ,  $ap\_r3-ap\_r4$ ,  $ap\_g5-ap\_g6$ ,  $ap\_g4-ap\_r4$ ,  $ap\_g6-ap\_g7$ ,  $ap\_g1-ap\_g2$ ,  $ap\_g3-ap\_g4$ ,  $ap\_g7-ap\_r7$ ,  $ap\_z5-ap\_z6$ ,  $ap\_g8-ap\_r8$ ,  $ap\_z7-ap\_z8$ ,  $ap\_z6-ap\_z7$ ,  $ap\_g2-ap\_g3$ ,  $ap\_r3-ap\_z3$ ,  $ap\_g7-ap\_g8$ ,  $ap\_r6-ap\_r7$ ,  $ap\_g3-ap\_r3$ ,  $ap\_r1-ap\_z1$ ,  $ap\_r7-ap\_r8$ ,  $ap\_g1-ap\_r1$ ,  $ap\_r5-ap\_r6$ ,  $ap\_g2-ap\_r2$ ,  $ap\_r2-ap\_z2$ ,  $ap\_z5-ap\_W15$ ,  $ap\_z2-ap\_W12$ ,  $ap\_W15-ap\_W25$ ,  $ap\_W14-ap\_W24$ ,  $ap\_W12-ap\_W22$ ,  $ap\_W11-ap\_W21$ ,  $ap\_W12-ap\_W13$ ,  $ap\_z4-ap\_W14$ ,  $ap\_z1-ap\_W11$ ,  $ap\_W13-ap\_W23$ ,  $W1-ap\_W11$ ,  $W2-ap\_W21$ ,  $ap\_W11-ap\_W12$ ,  $ap\_W24-ap\_W25$ ,  $ap\_W23-ap\_W24$ ,  $ap\_W22-ap\_W23$ ,  $ap\_W21-ap\_W22$ ,  $ap\_W14-ap\_W15$ ,  $ap\_W13-ap\_W14$ ,  $ap\_z3-ap\_W13$ . (60 features).

Pattern III is  $r-W1$ ,  $g-r$ ,  $g$ ,  $r$ ,  $r-z$ ,  $W1-W2$ ,  $ap\_r4-ap\_z4$ ,  $ap\_g5-ap\_r5$ ,  $z-ap\_z1$ ,  $W1$ ,  $r-W2$ ,  $ap\_r6-ap\_z6$ ,  $z$ ,  $g-ap\_g1$ ,  $ap\_z4-ap\_z5$ ,  $r-ap\_r1$ ,  $ap\_z1-ap\_z2$ ,  $g-W1$ ,  $ap\_r1-ap\_r2$ ,  $g-z$ ,  $ap\_r4-ap\_r5$ ,  $ap\_g6-ap\_r6$ ,  $ap\_r7-ap\_z7$ ,  $ap\_z2-ap\_z3$ ,  $ap\_r5-ap\_z5$ ,  $ap\_r8-ap\_z8$ ,  $ap\_g4-ap\_g5$ ,  $W2$ ,  $g-W2$ ,  $ap\_z3-ap\_z4$ ,  $ap\_r2-ap\_r3$ ,  $ap\_r3-ap\_r4$ ,  $ap\_g5-ap\_g6$ ,  $ap\_g4-ap\_r4$ ,  $ap\_g6-ap\_g7$ ,  $ap\_g1-ap\_g2$ ,  $ap\_g3-ap\_g4$ ,  $ap\_g7-ap\_r7$ ,  $ap\_z5-ap\_z6$ ,  $ap\_g8-ap\_r8$ ,  $ap\_z7-ap\_z8$ ,  $ap\_z6-ap\_z7$ ,  $ap\_g2-ap\_g3$ ,  $ap\_r3-ap\_z3$ ,  $ap\_g7-ap\_g8$ ,  $ap\_r6-ap\_r7$ ,  $ap\_g3-ap\_r3$ ,  $ap\_r1-ap\_z1$ ,  $ap\_r7-ap\_r8$ ,  $ap\_g1-ap\_r1$ ,  $ap\_r5-ap\_r6$ ,  $ap\_g2-ap\_r2$ ,  $ap\_r2-ap\_z2$ , (53 features).